Reaction Kinetics, Mechanisms and Catalysis (2021) 134:711–725
https://doi.org/10.1007/s11144-021-02085-7

Oxidative coupling of methane over Y_2O_3 and Sr–Y_2O_3 nanorods

Yuqiao Fan[1] · Changxi Miao[2] · Yinghong Yue[1] · Weiming Hua[1] · Zi Gao[1]

Received: 16 August 2021 / Accepted: 12 October 2021 / Published online: 24 October 2021

Abstract

Y_2O_3 nanorods were prepared via a hydrothermal method. A series of Sr-modified Y_2O_3 nanorods (Sr–Y_2O_3–NR) with a Sr/Y molar ratio of 0.02–0.06 were synthesized by an impregnation method, and studied with respect to their performance in the oxidative coupling of methane (OCM). The structural and physicochemical properties of these catalysts were characterized by means of XRD, N_2 adsorption, SEM, TEM, XPS, O_2-TPD and CO_2-TPD. Y_2O_3 nanorods exhibit higher CH_4 conversion and C_2–C_3 selectivity relative to Y_2O_3 nanoparticles, which could link with the fact that Y_2O_3 nanorods predominantly expose (440) and (222) planes. The addition of a small amount of Sr to Y_2O_3 nanorods enhances the activation of oxygen, the ratio of $(O^- + O_2^-)/O^{2-}$ and amount of moderate basic sites for the Sr–Y_2O_3-NR catalysts, thus promoting the OCM performance. The best 0.04Sr–Y_2O_3-NR catalyst with a Sr/Y molar ratio of 0.04 can give a 23.0% CH_4 conversion with 50.2% C_2–C_3 selectivity at 650 °C. We found that the C_2–C_3 yield achieved on the Y_2O_3-based catalysts correlated well with the amount of moderate basic sites present on the catalysts.

Keywords Oxidative coupling of methane · Y_2O_3-based nanorods · Morphology effect · Sr modification

Introduction

Catalytic conversion of methane to value added products has attracted much attention in the past few decades [1–13]. The proven reserve of natural gas, with its major component CH_4, has increased markedly from 1996 to 2016, and therefore providing

✉ Weiming Hua
wmhua@fudan.edu.cn

[1] Shanghai Key Laboratory of Molecular Catalysis and Innovative Materials, Department of Chemistry, Fudan University, Shanghai 200438, People's Republic of China

[2] Shanghai Research Institute of Petrochemical Technology SINOPEC, Shanghai 201208, People's Republic of China

great motivation in methane utilization. There is no doubt that oxidative coupling of methane (OCM) is one of the most prospective directions among the various conversion of methane, since Keller et al. [14] first reported this technology in 1982. The main products of OCM reaction are ethane and ethylene. Ethylene, one of the chemical products with the largest output in the world, has been regarded as one of the important indicators to measure the development level of a country's petrochemical industry [15]. Hence, a wide range of catalysts have been attempted on the OCM reaction [1, 2, 7, 10].

Recently, researchers have shifted the focus of study to the OCM process at relatively low temperatures. It is worth noting that rare earth oxide catalysts with special morphologies (e.g. nanorods, nanobelts and nanowires) such as La_2O_3 [16, 17], Sm_2O_3 [18] and CeO_2 [19] can effectively catalyze low-temperature OCM reaction at 500–650 °C. To improve the C_2 selectivity of OCM reaction, mixed or doped oxides with enhanced basicity such as alkali-rare earth oxides [20] and alkaline earth-rare earth oxides [21–23] were used. In addition to the basicity, introducing the low-valence metal into high-valence metal oxides can produce the surface defects to form electrophilic oxygen species such as O^- and O_2^- which are conductive to improving the C_2 selectivity. More recently, we have found that Er_2O_3 nanorods, Ho_2O_3 nanosheets and their Sr-promoted forms can act as effective catalysts for low-temperature OCM process [24, 25].

Takenaka et al. found that Li-added Y_2O_3 was the most effective catalyst for the OCM reaction among various basic metal oxide catalysts (MgO, Y_2O_3, La_2O_3, Gd_2O_3, Sm_2O_3, Eu_2O_3 and CeO_2) modified with Li [20]. Although Y_2O_3-based catalysts used in the OCM reaction were reported, their catalytic performance at relatively low temperature was not satisfactory [20, 26–28]. Inspired by the aforementioned research results [16–19, 24, 25], in the present work we have developed Y_2O_3 and Sr-modified Y_2O_3 nanorods used as efficient catalysts for low-temperature OCM process. The catalytic performance of these catalysts was correlated with their characterization results.

Experimental

Catalyst preparation

Y_2O_3 nanorods (named as Y_2O_3-NR) were synthesized by a hydrothermal method. In a typical procedure, 3.83 g of $Y(NO_3)_3 \cdot 6H_2O$ was dissolved in 100 mL deionized water. 5 mL aqueous ammonia (25–28 wt%) was then added dropwise to $Y(NO_3)_3$ solution under stirring. The resulting suspension was transferred into a Teflon-lined stainless autoclave, followed by being placed in an oven setting at 200 °C for 12 h. Y_2O_3 nanoparticles (labelled as Y_2O_3-NP) were synthesized by a conventional precipitate method. 3 mL aqueous ammonia (25–28 wt%) was added dropwise to 100 mL $Y(NO_3)_3$ solution (0.1 M) under stirring. All the obtained precipitates were fully washed with deionized water, dried at 80 °C for 12 h. Finally, the dried $Y(OH)_3$ samples were calcined at 750 °C in air for 4 h to obtain Y_2O_3 nanorods and nanoparticles.

Sr-modified Y_2O_3 nanorods were synthesized by an incipient wetness impregnation method. Different amounts of $Sr(NO_3)_2$ were dissolved in deionized water, and then a certain amount of dried $Y(OH)_3$ nanorods were added. After drying under an infrared lamp, the sample was dried at 80 °C for 12 h, then calcined at 750 °C in air for 4 h. The obtained catalysts were designated as xSr–Y_2O_3-NR, which x represents the Sr/Y molar ratio ($x=0.02$, 0.04 and 0.06).

Catalyst characterization

X-ray diffraction (XRD) patterns were recorded on a D2 PHASER X-ray diffractometer using nickel-filtered Cu K_α radiation at 30 kV and 10 mA. The BET surface areas of the catalysts were measured by N_2 adsorption at − 196 °C using a Micromeritics Tristar 3000 instrument. X-ray photoelectron spectroscopy (XPS) analyses were carried out with a Perkin–Elmer PHI 5000C spectrometer. All binding energy values were calibrated using the C 1 s peak at 284.6 eV. Field-emission scanning electron microscopy (FESEM) images were taken using a Hitachi S-4800 instrument. Transmission electron microscopy (TEM) images were recorded on an FEI Tecnai G^2 F20 S-TWIN instrument. Fourier transform infrared (FTIR) spectra were measured on a Nicolet Avatar 360 spectrometer. 20 mg of spent catalyst and 200 mg of KBr were first mixed uniformly. 30 mg of mixture was then pressed into a self-supporting disk.

The amount and strength of basic sites were measured by CO_2 temperature programmed desorption (CO_2-TPD) using a Micromeritics AutoChem II analyzer. 0.2 g of catalyst (40–60 mesh) was preheated at 750 °C for 1 h under He (30 mL/min), followed by cooling down to 80 °C. CO_2 adsorption was conducted at this temperature, then purged with He (30 mL/min) for 2 h. Finally, the temperature was raised from 80 to 950 °C at a ramping rate of 10 °C/min. O_2 temperature programmed desorption (O_2-TPD) was measured on the same instrument. 0.2 g of catalyst (40–60 mesh) was preheated at 750 °C for 1 h under He (30 mL/min), followed by cooling down to 50 °C. O_2 adsorption was conducted at this temperature, then purged with He (30 mL/min) for 2 h. Finally, the temperature was then raised from 50 to 700 °C at a ramping rate of 10 °C/min. The desorbed CO_2 and O_2 were detected with a thermal conductivity detector (TCD).

Oxidative coupling of methane

The oxidative coupling of methane reaction was performed with a fixed-bed quartz tube reactor (internal diameter 6 mm) at atmospheric pressure. 0.2 g of catalyst (40–60 mesh) was loaded in the middle of reactor, with the downstream of the catalyst fixed with quartz wool. The catalytic performance was investigated using a gas mixture of methane and oxygen ($CH_4/O_2=4/1$ molar ratio). The total flow rate of 60 mL/min, corresponding to a gas hourly space velocity (GHSV) of 18,000 mL/(g h). Prior to the reaction, the catalyst was pretreated at 750 °C in Ar (30 mL/min) for 1 h. The reaction temperature (actually the catalyst bed temperature) was monitored by a thermocouple placed in the middle of the catalyst bed. The reaction products were analyzed by an on-line GC equipped with a TCD and a 2-m Shincarbon ST packed column (for separation of H_2, O_2, CO, CH_4 and CO_2), and by another on-line GC equipped with an FID and a 50-m PoraPLOT Q capillary column (for separation of CH_4, C_2H_4, C_2H_6, C_3H_6 and C_3H_8). Before analyzing by TCD, the products were passed through a cold trap at -3 °C to remove most of water generated during the reaction. The CH_4 conversion and C_2-C_3 selectivity were calculated using the standard normalization method based on carbon atom balance.

Results and discussion

Catalyst characterization

The XRD patterns of Y_2O_3 nanoparticles, nanorods and Sr-modified nanorods are shown in Fig. 1. All catalysts display similar characteristics of diffraction peaks belonging to the cubic Y_2O_3 phase (PDF #74–1828). The diffraction peaks at ca. $2\theta = 21°$, 29°, 34°, 36.1°, 40°, 44°, 49°, 54°, 58° and 59° are ascribed to the (211), (222), (400), (411), (332), (134), (440), (611), (622) and (136) planes of cubic Y_2O_3 phase. As the Sr/Y molar ratio is increased to 0.04, a small amount of $SrCO_3$ phase appeared, which might be produced during the calcination of $Sr(NO_3)_2$-$Y(OH)_3$ through the combination of SrO with CO_2 in air [22, 29]. Table 1 shows that introducing a small amount of Sr into Y_2O_3 nanorods improves the lattice parameter from 1.0546 nm (Y_2O_3-NR) to 1.0569 nm (0.06Sr–Y_2O_3-NR). Taking into account the larger ionic radius of Sr^{2+} (0.118 nm) than Y^{3+} (0.090 nm), this result reveals that Sr is doped into the crystal lattice of Y_2O_3, albeit Sr was incorporated into Y_2O_3 nanorods via a simple impregnation method [22, 29].

From the SEM images of Y_2O_3-NR (Fig. 2a) and 0.04Sr–Y_2O_3-NR (Fig. 2b), one can see that both catalysts show the nanorod shape. The average length and width of Y_2O_3-NR nanorods are 1.11 μm and 191 nm, respectively. Obviously, the introduction of a small amount of Sr exerts a bit influence on the nanorod size (Table 1). The TEM image shown in Fig. 3 indicates that Y_2O_3-NP has irregular particle shape with a mean size of 17 nm. As demonstrated in Figs. S1 and S2, the HR-TEM images

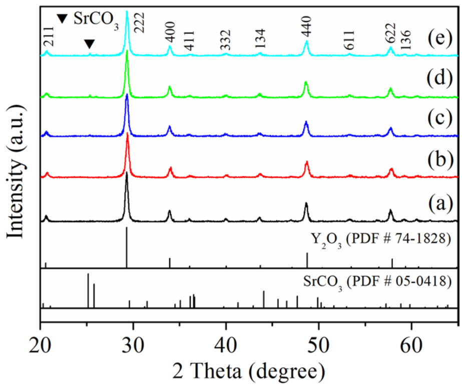

Fig. 1 XRD patterns of **a** Y_2O_3–NP; **b** Y_2O_3–NR; **c** 0.02Sr–Y_2O_3–NR; **d** 0.04Sr–Y_2O_3–NR; **e** 0.06Sr–Y_2O_3–NR

Table 1 Textural properties and XPS data of the Y_2O_3-based catalysts

Catalyst	S_{BET} (m^2/g)	Average size (μm)	$a=b=c$ (nm)[d]	O 1 s BE[e], FWHM[f] (eV) O^{2-}	O^-	CO_3^{2-}	O_2^-	$(O^- + O_2^-)/O^{2-}$
Y_2O_3-NP	20.0	0.017 ± 0.003	1.0544	529.4/1.7	530.7/1.4	531.7/1.3	532.6/1.3	1.0
Y_2O_3-NR	25.4	1.11 ± 0.25[a] 0.191 ± 0.033[b]	1.0546	529.5/1.4	530.4/1.3	531.6/1.4	532.6/1.7	1.3
0.02Sr-Y_2O_3-NR	24.0	–[c]	1.0556	529.6/1.4	530.6/1.5	531.9/1.4	532.8/1.4	1.5
0.04Sr-Y_2O_3-NR	20.1	1.09 ± 0.20[a] 0.196 ± 0.032[b]	1.0563	529.3/1.4	530.4/1.7	531.6/1.3	532.5/1.4	1.8
0.06Sr-Y_2O_3-NR	20.0	–[c]	1.0569	529.6/1.4	530.6/1.5	531.8/1.3	532.7/1.5	1.6

[a]Average length of the nanorods

[b]Average width of the nanorods

[c]Not measured

[d]Lattice parameter

[e]Binding energy

[f]Full width at half maximum

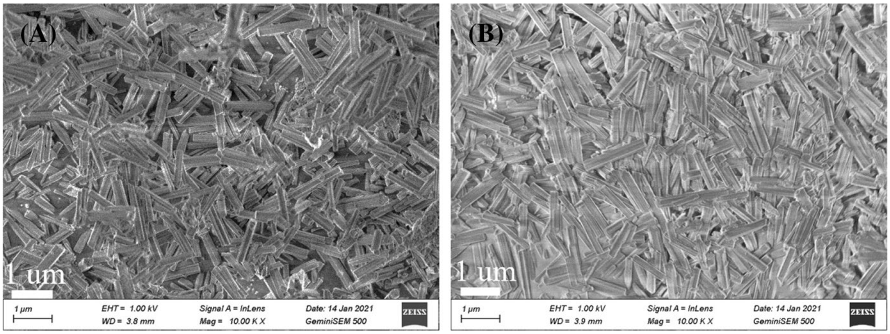

Fig. 2 SEM images of **A** Y_2O_3–NR; **B** 0.04Sr–Y_2O_3–NR

Fig. 3 TEM image of Y_2O_3–NP

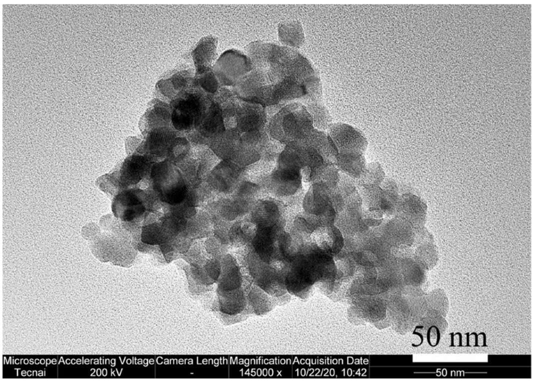

combined with a fast Fourier transform (FFT) analysis disclose that Y_2O_3-NR and 0.04Sr-Y_2O_3-NR nanorods predominantly expose (440) and (222) planes.

The BET specific surface areas of Y_2O_3 nanoparticles, nanorods and Sr-modified nanorods are between 20.0 and 25.4 m^2/g (Table 1), which are low and typical for the OCM catalysts. Y_2O_3-NR presents a slightly higher surface area than Y_2O_3-NP (25.4 vs 20.0 m^2/g). Modification of Y_2O_3-NR with a small amount of Sr brings about a slight decrease in surface area.

The XPS spectra of O 1 s on the Y_2O_3-based catalysts are shown in Fig. S3. The O 1 s spectrum of each catalyst can be deconvoluted into four peaks associated with three kinds of oxygen species: lattice oxygen (O^{2-}, ~ 529.4 eV), chemisorbed oxygen species (O^-, ~ 530.6 eV and O_2^-, ~ 532.6 eV) and carbonate (CO_3^{2-}, ~ 531.8 eV) [16, 30–33]. The XPS data are presented in Table 1. It was reported that the chemisorbed oxygen species, i.e. surface electrophilic oxygen species O^- and O_2^-, were responsible for the generation of C_2 product in the OCM process, while the lattice oxygen favored deep oxidation of CH_4 to form CO and CO_2 [16, 17, 22, 32, 34]. Hence, the ratio of $(O^- + O_2^-)/O^{2-}$ was found to correlate positively with C_2 selectivity in the OCM reaction [17, 22, 25, 29, 34]. A comparison of Y_2O_3-NR with Y_2O_3-NP indicates that the former catalyst affords a higher ratio of $(O^- + O_2^-)/O^{2-}$ than the latter one (1.3 vs 1.0). Introducing Sr into Y_2O_3-NR increases the $(O^- + O_2^-)/O^{2-}$ ratio, and the 0.04Sr-Y_2O_3-NR catalyst exhibits the highest value (1.8). Apparently, the value of $(O^- + O_2^-)/O^{2-}$ for all the Y_2O_3-based catalysts follows the sequence of 0.04Sr–Y_2O_3-NR > 0.06Sr–Y_2O_3-NR > 0.02Sr–Y_2O_3-NR > Y_2O_3-NR > Y_2O_3-NP.

A previous theoretical study has revealed that the energy required to produce oxygen vacancies over CeO_2 is lower on the plane of (110) than (111) and (310) [35]. That is to say, oxygen vacancies are more readily to generate on the (110) plane of CeO_2. Oxygen vacancies can interact with O_2 to form the chemisorbed oxygen species such as O^- and O_2^-. Hou et al. pointed out that, among the exposed facets for the $La_2O_2CO_3$ catalysts, the (110), $(1\,\bar{2}\,0)$ and $(2\,\bar{1}\,0)$ facets had relatively loose atomic configurations, and these facets favored the formation of the chemisorbed oxygen species [33]. Thus, we consider that the higher $(O^- + O_2^-)/O^{2-}$ ratio for Y_2O_3-NR than Y_2O_3-NP could be caused by the fact that the former catalyst predominantly exposes (440) and (222) planes, as revealed by the HR-TEM result.

The activation of oxygen will play an important role in the OCM reaction. To further study the oxygen activation on the Y_2O_3-based catalysts, O_2-TPD experiments were performed. The results are given in Fig. 4 and Table 2. The Y_2O_3-NP catalyst gives two desorption peaks of oxygen, which are located at 93 °C and 526 °C, respectively. The low-temperature and high-temperature peaks are assigned to molecular and chemisorbed oxygen species, respectively [36]. The other Y_2O_3-based catalysts display only one peak of oxygen desorption located at 370–507 °C, which corresponds to the desorption of chemisorbed oxygen species [36]. These chemisorbed oxygen species originate from the interaction between O_2 and the Y_2O_3-based catalysts, and may be O^-, O_2^- and O^{2-} [29, 33]. It is widely accepted that the chemisorbed oxygen species are helpful for CH_4 activation and C_2 selectivity in the OCM reaction [16, 33, 36, 37]. In comparison with Y_2O_3-NP, Y_2O_3-NR displays a higher amount of chemisorbed oxygen species (25.8 vs 21.0 μmol/g). Compared with Y_2O_3-NR, the Sr–Y_2O_3-NR catalysts possess a higher amount of

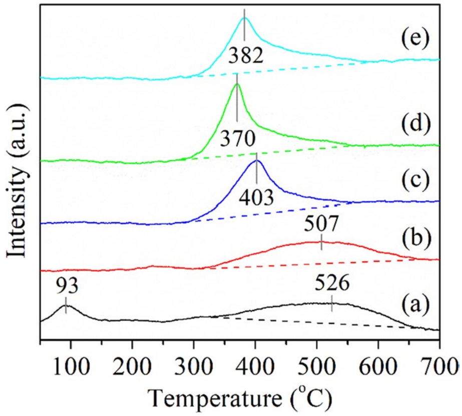

Fig. 4 O_2-TPD profiles of **a** Y_2O_3–NP; **b** Y_2O_3–NR; **c** 0.02Sr–Y_2O_3–NR; **d** 0.04Sr–Y_2O_3–NR; **e** 0.06Sr–Y_2O_3-NR

Table 2 O_2-TPD and CO_2-TPD data of the Y_2O_3-based catalysts

Catalyst	Peak temperature (°C)		Amount of desorbed O_2 (μmol/g)		Amount of basic sites[a] (μmol/g)		
	I	II	I	II	Weak	Moderate	Strong
Y_2O_3-NP	93	526	3.5	21.0	2.3	6.6	–
Y_2O_3-NR	–	507	–	25.8	4.1	22.4	–
0.02Sr–Y_2O_3-NR	–	403	–	36.3	3.7	42.6	19.6
0.04Sr–Y_2O_3-NR	–	370	–	43.7	3.3	47.9	91.1
0.06Sr–Y_2O_3-NR	–	382	–	39.2	3.1	44.9	144.7

[a]The temperature range for weak, intermediate and strong basic sites is 80–200 °C, 200–575 °C and 650–950 °C

chemisorbed oxygen species (36.3–43.7 vs 25.8 μmol/g) and lower peak temperature of the chemisorbed oxygen species desorption (370–403 °C vs 507 °C). The 0.04Sr–Y_2O_3-NR catalyst affords the highest amount of chemisorbed oxygen species (43.7 μmol/g). This finding suggests that the incorporation of a small amount of Sr into Y_2O_3 nanorods enhances the oxygen activation over the catalysts. Doping low-valence Sr into high-valence Y_2O_3 can improve the number of oxygen vacancies [37–39], thus enhancing the activation of oxygen. Consequently, a higher amount of chemisorbed oxygen species on the Sr–Y_2O_3-NR catalysts than Y_2O_3-NR can be observed.

Surface basic sites were also considered to play a key role in the OCM reaction [21, 40]. These basic sites could be O^-, O_2^- and O^{2-} oxygen species [21, 37, 41, 42]. The basic sites with medium strength are considered to be more favorable for forming C_2 product in the OCM reaction [16, 17, 25, 33, 40, 43–46]. The CO_2-TPD profiles of Y_2O_3 nanoparticles, nanorods and Sr-modified nanorods are depicted in Fig. 5. There are three peaks of CO_2 desorption from the surfaces of Sr-modified Y_2O_3 nanorods, which are located at ~ 150 °C, ~ 340 °C

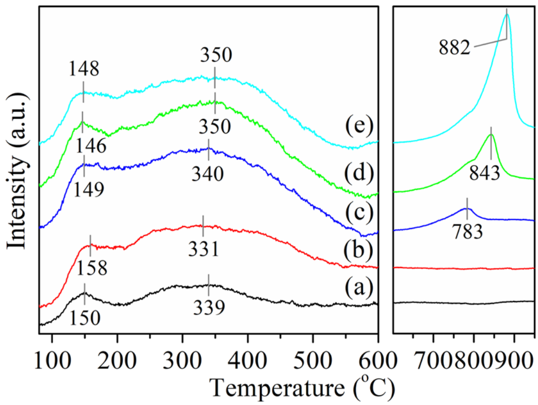

Fig. 5 CO_2-TPD profiles of **a** Y_2O_3–NP; **b** Y_2O_3–NR; **c** 0.02Sr–Y_2O_3–NR; **d** 0.04Sr–Y_2O_3–NR; **e** 0.06Sr–Y_2O_3–NR. The signal of each catalyst on the left part was magnified six times

and above 750 °C, corresponding to weak, moderate and strong basic sites of the catalysts [22, 29, 37, 47]. Both Y_2O_3-NR and Y_2O_3-NP catalysts have only weak and moderate basic sites, giving the peak temperature of CO_2 desorption at ~ 150 °C and ~ 340 °C. The CO_2-TPD data (Table 2) show that the amount of moderate basic sites is higher over Y_2O_3-NR than Y_2O_3-NP. The Sr–Y_2O_3-NR catalysts possess more basic sites with medium strength than Y_2O_3-NR, and 0.04Sr–Y_2O_3-NR has the greatest amount of moderate basic sites. The amount of moderate basic sites present on all the Y_2O_3-based catalysts decreases in the order of 0.04Sr–Y_2O_3-NR > 0.06Sr–Sr–Y_2O_3-NR > 0.02Sr–Y_2O_3-NR > Y_2O_3-NR > Y_2O_3-NP.

FTIR spectra can provide the information on structure of the catalysts. To gain insight into the impact of introducing excessive Sr on the Sr–Y_2O_3-NR catalysts for the OCM process, the used 0.06Sr–Y_2O_3-NR and 0.04Sr–Y_2O_3-NR catalysts after the OCM reaction at 600 °C for 1 h were recorded and compared in Fig. S4. The peaks located at 3445 and 1637 cm^{-1} are attributed to the stretching and bending vibrations of O–H groups in H_2O [48]. The peaks centered at 1442 and 861 cm^{-1} are assigned to the asymmetric stretching and bending vibrations of CO_3^{2-} groups [49, 50] which originate from combination of the Sr–Y_2O_3-NR catalysts with CO_2 produced in the OCM process. Judging from the peak intensity, there are more surface carbonate species on the spent catalysts of 0.06Sr–Y_2O_3-NR than 0.04Sr–Y_2O_3-NR.

Catalytic performance

To explore the morphology effect of the Y_2O_3 catalysts, we first tested the catalytic performance of Y_2O_3 nanorods and nanoparticles. With an increase of the reaction temperature from 600 to 750 °C, the CH_4 conversion increases slightly (Fig. 6A), while the selectivity toward C_2–C_3 (ethylene, ethane, propylene and propane) increases significantly (Fig. 6B). Accordingly, the C_2–C_3 yield rises with the reaction temperature (Fig. 6C). Whether CH_4 conversion, C_2–C_3 selectivity or C_2–C_3 yield, Y_2O_3-NR performs better than Y_2O_3-NP. For example, Y_2O_3-NR affords a 21.9% CH_4 conversion, 42.3% C_2–C_3 selectivity and 9.3% C_2–C_3 yield at 700 °C, whereas Y_2O_3-NP gives a 17.9% CH_4 conversion, 22.9%

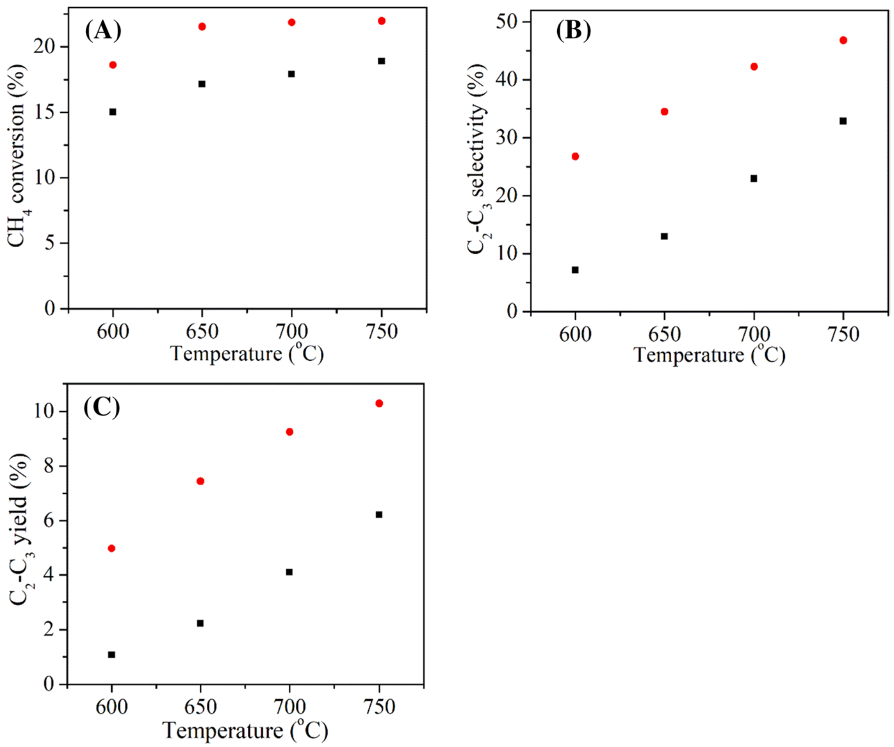

Fig. 6 CH_4 conversion (**A**), C_2–C_3 selectivity (**B**) and C_2–C_3 yield (**C**) as a function of reaction temperature for the Y_2O_3 catalysts: (filled square) Y_2O_3–NP; (filled circle) Y_2O_3–NR. Reaction conditions: 0.2 g catalyst, 60 mL/min flow (molar ratio $CH_4/O_2 = 4/1$)

C_2–C_3 selectivity and 4.1% C_2–C_3 yield. A higher C_2–C_3 selectivity achieved on Y_2O_3-NR than Y_2O_3-NP is caused by a higher $(O^- + O_2^-)/O^{2-}$ ratio obtained on the former catalyst. The occurrence of more chemisorbed oxygen species and moderate basic sites on Y_2O_3-NR than Y_2O_3-NP is responsible for a higher CH_4 conversion and C_2–C_3 yield achieved on the former catalyst. The La_2O_3, Sm_2O_3, Er_2O_3 and Ho_2O_3 rare earth oxide catalysts were also found to display shape effects on the OCM reaction [16–18, 24, 25].

Then we tested the catalytic performance of Sr–Y_2O_3-NR catalysts to get a better understanding of the influence of Sr modification. Table 3 shows the typical product distribution over the Y_2O_3-NR and Sr–Y_2O_3-NR catalysts at 650 °C. In addition to C_2H_4 and C_2H_6, small amounts of C_3H_6 and C_3H_8 were also produced. As to the by-products, the selectivity is higher for CO_2 than CO. Compared with the Y_2O_3-NR catalyst, the addition of a small amount of Sr slightly improves the CH_4 conversion (Fig. 7A), and obviously enhances the C_2–C_3 selectivity (Fig. 7B) and yield (Fig. 7C). With an increase of the Sr/Y molar ratio from 0 to 0.06, the CH_4 conversion, C_2–C_3 selectivity and yield first increase and then decrease. The best catalytic performance is achieved on the 0.04Sr–Y_2O_3-NR

Table 3 Reaction data of the Y_2O_3–NR and Sr–Y_2O_3–NR catalysts at 650 °C[a]

Catalyst	CH_4 Conv. (%)	Selectivity (%) C_2H_4	C_2H_6	C_3H_6	C_3H_8	CO_2	CO	C_2–C_3 Select. (%)	C_2–C_3 Yield (%)
Y_2O_3–NR	21.5	16.4	16.4	0.7	1.0	51.1	14.4	34.5	7.4
0.02Sr–Y_2O_3–NR	21.9	24.3	20.6	1.1	1.3	42.3	10.4	47.3	10.4
0.04Sr–Y_2O_3–NR	23.0	24.5	23.0	1.3	1.4	41.0	8.8	50.2	11.5
0.06Sr–Y_2O_3–NR	22.1	21.9	20.8	1.2	1.5	45.0	9.6	45.4	10.0

[a]Reaction conditions: 0.2 g catalyst, 60 mL/min flow (molar ratio $CH_4/O_2 = 4/1$)

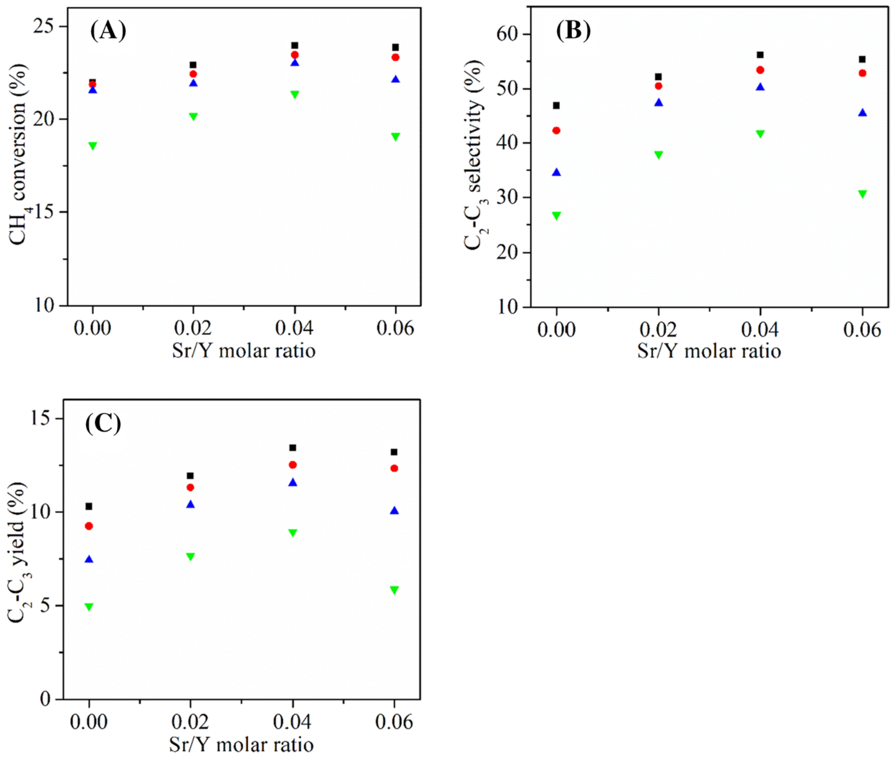

Fig. 7 Effect of Sr/Y molar ratio on the catalytic behavior of Sr-modified Y_2O_3 nanorods at different temperatures: **A** CH_4 conversion, **B** C_2–C_3 selectivity and **C** C_2–C_3 yield. (inverted triangle) 600 °C, (triangle) 650 °C, (filled circle) 700 °C, (filled square) 750 °C. Reaction conditions: 0.2 g catalyst, 60 mL/min flow (molar ratio $CH_4/O_2 = 4/1$)

catalyst, which affords a 23.0% CH_4 conversion and 50.2% C_2-C_3 selectivity at 650 °C. Even at a low temperature of 600 °C, this catalyst still gives a 21.4% CH_4 conversion and 41.8% C_2–C_3 selectivity. In contrast, the Y_2O_3-NR catalyst only affords a 21.5% CH_4 conversion and 34.5% C_2–C_3 selectivity at 650 °C. In combination with the above XPS, O_2-TPD and CO_2-TPD results, the better OCM performance of the Sr–Y_2O_3-NR catalysts than Y_2O_3-NR can be attributed to an increased $(O^- + O_2^-)/O^{2-}$ ratio and number of moderate basic sites, as well as enhanced activation of oxygen. The best 0.04Sr–Y_2O_3-NR catalyst display the highest ratio of $(O^- + O_2^-)/O^{2-}$ as well as the most chemisorbed oxygen species and moderate basic sites. As revealed in Fig. 8, there exists a good correlation between the C_2–C_3 yield achieved on the Y_2O_3-based catalysts at 700 °C and the number of moderate basic sites present on the catalysts. This finding further demonstrates that the presence of moderate basic sites on the OCM catalysts is conducive to improving the C_2 yield [16, 17, 25, 33, 40, 43–46].

A bit lower CH_4 conversion and C_2–C_3 selectivity can be found on 0.06Sr–Y_2O_3-NR than 0.04Sr–Y_2O_3-NR at 750 °C and 700 °C, which could link with the blockage of some active sites upon the addition of excessive Sr. An interesting observation is that the former catalyst displays obviously worse OCM performance than the latter one at 650 °C and 600 °C, especially at a low temperature of 600 °C. This can be attributed to the blockage of more active sites by carbonate, since more surface carbonate species are formed on the spent 0.06Sr–Y_2O_3-NR catalyst (Fig. S4). Reportedly, there existed the optimal Li and Ba contents for Li–MgO and Ba–La_2O_3 catalysts used in the OCM process [51, 52].

We chose the best 0.04Sr–Y_2O_3-NR catalyst to investigate the lifetime for the OCM reaction performed at 650 °C. As seen in Fig. S5, the 0.04Sr–Y_2O_3-NR catalyst displays good stability during 60 h of reaction, maintaining around 23% CH_4 conversion and 50% C_2–C_3 selectivity. As demonstrated in Fig. S6, the HR-TEM images combined with a fast Fourier transform (FFT) analysis indicate that the predominantly exposed surface facets observed for 0.04Sr–Y_2O_3-NR after the stability test are not altered. After the stability test, the SEM image of 0.04Sr–Y_2O_3-NR displays the nanorod shape with an average length of 1.10 μm and width of 190 nm (Fig. S7). The 0.04Sr–Y_2O_3-NR catalyst possesses a surface area of 19.9 m^2/g and 43.4 μmol/g of chemisorbed oxygen species. The amount of weak, moderate and strong basic sites of spent 0.04Sr-Y_2O_3-NR is 3.3, 47.6 and 90.7 μmol/g. The characterization data obtained for 0.04Sr–Y_2O_3-NR after the stability test are equivalent to those of the fresh catalyst, indicating the maintenance of the catalyst structure during the reaction.

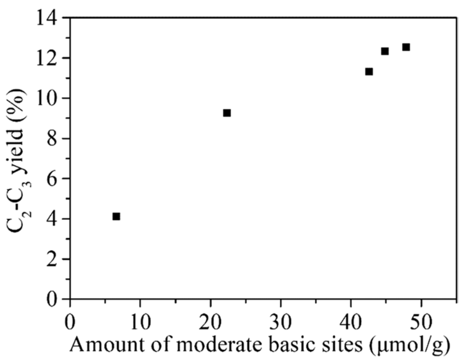

Fig. 8 Relationship between the C_2–C_3 yield achieved at 700 °C and the amount of moderate basic sites over the Y_2O_3-based catalysts. Reaction conditions: 0.2 g catalyst, 60 mL/min flow (molar ratio $CH_4/O_2 = 4/1$)

We compared catalytic performance of our catalyst 0.04Sr–Y_2O_3-NR and three reference catalysts, i.e. 0.04Ba–Y_2O_3-NR nanorods, 0.04Sr–La_2O_3-NF nanofibers [22] and 0.04Sr–Sm_2O_3-NB nanobelts [18], under our reaction conditions. As shown in Fig. S8. Our catalyst 0.04Sr–Y_2O_3-NR displays higher methane conversion than 0.04Sr–La_2O_3-NF, and lower conversion than 0.04Ba–Y_2O_3-NR and 0.04Sr–Sm_2O_3-NB. However, 0.04Sr–Y_2O_3-NR nanorods exhibit a bit greater C_2–C_3 yield than three reference catalysts at 600–750 °C. Recently, Sollier et al. has reported that Sr–La–Ce oxide fibers reached a C_2 yield of 21.7% at 600 °C [53]. In our future work we will study the effect of Ce doping on the Sr–Y_2O_3-NR nanorods.

Conclusions

In this work, we have developed Y_2O_3 and Sr–Y_2O_3 nanorods as new catalysts for low-temperature OCM process. The HR-TEM images reveal that Y_2O_3 and Sr–Y_2O_3 nanorods preferentially expose (440) and (222) facets. The superior OCM performance of Y_2O_3 nanorods to their nanoparticles counterpart could be associated with the predominantly exposed (440) and (222) facets on the surface of Y_2O_3 nanorods. The XPS and CO_2-TPD results indicate that the addition to a small amount of Sr to Y_2O_3 nanorods enhances the ratio of $(O^- + O_2^-)/O^{2-}$ and amount of moderate basic sites. The O_2-TPD result suggests that the Sr addition promotes the activation of oxygen on the Sr–Y_2O_3-NR catalysts. This enhancement and promotion lead to an improved catalytic performance of Y_2O_3 nanorods upon the introduction of Sr. The optimal 0.04Sr–Y_2O_3-NR nanorods with a Sr/Y molar ratio of 0.04 afford a 23.0% CH_4 conversion and 50.2% C_2–C_3 selectivity at 650 °C. This catalyst displays good stability for 60 h of OCM reaction. We found that there existed a good correlation between the C_2–C_3 yield achieved on the Y_2O_3-based catalysts and the number of moderate basic sites present on the catalysts.

Supplementary Information The online version contains supplementary material available at https://doi.org/10.1007/s11144-021-02085-7.

Acknowledgements Financial support of this work was provided by the National Key R&D Program of China (No. 2017YFB0602200), the National Natural Science Foundation of China (No. 91645201), the Science and Technology Commission of Shanghai Municipality (No. 19DZ2270100), and the Shanghai Research Institute of Petrochemical Technology SINOPEC (No. 33750000-19-ZC0607-0005).

Author contributions WH, CM: Conceptualization; WH, YY: Methodology; YF: Formal analysis and investigation; YF: Writing—original draft preparation; WH, ZG: Writing—review and editing; WH, CM:Supervision.

Declarations

Conflict of interest The authors declare no conflict of interest.

Data availability The datasets of current study are available from the corresponding authors on reasonable request.

References

1. Lee J, Oyama S (1988) Oxidative coupling of methane to higher hydrocarbons. Catal Rev Sci Eng 30(2):249–280
2. Arndt S, Laugel G, Levchenko S, Horn R, Baerns M, Scheffler M, Schlögl R, Schomäcker R (2011) A critical assessment of Li/MgO-based catalysts for the oxidative coupling of methane. Catal Rev Sci Eng 53(4):424–514
3. Ge XM, Yang LC, Sheets JP, Yu ZT, Li YB (2014) Biological conversion of methane to liquid fuels: status and opportunities. Biotechnol Adv 32(8):1460–1475
4. Tang P, Zhu QJ, Wu ZX, Ma D (2014) Methane activation: the past and future. Energy Environ Sci 7(8):2580–2591
5. Taifan W, Baltrusaitis J (2016) CH_4 conversion to value added products: potential, limitations and extensions of a single step heterogeneous catalysis. Appl Catal B 198:525–547
6. Zakaria Z, Kamarudin SK (2016) Direct conversion technologies of methane to methanol: an overview. Renew Sust Energ Rev 65:250–261
7. Galadima A, Muraza O (2016) Revisiting the oxidative coupling of methane to ethylene in the golden period of shale gas: a review. J Ind Eng Chem 37:1–13
8. Han B, Yang Y, Xu Y, Etim UJ, Qiao K, Xu B, Yan Z (2016) A review of the direct oxidation of methane to methanol. Chin J Catal 37(8):1206–1215
9. Schwach P, Pan XL, Bao XH (2017) Direct conversion of methane to value-added chemicals over heterogeneous catalysts: challenges and prospects. Chem Rev 117(13):8497–8520
10. Gambo Y, Jalil AA, Triwahyono S, Abdulrasheed AA (2018) Recent advances and future prospect in catalysts for oxidative coupling of methane to ethylene: a review. J Ind Eng Chem 59:218–229
11. Zhao GY, Drewery M, Mackie J, Oliver T, Kennedy EM, Stockenhuber M (2020) The catalyzed conversion of methane to value-added products. Energy Technol 8(8):1900665
12. Sun LL, Wang Y, Guan NJ, Li LD (2020) Methane activation and utilization: current status and future challenges. Energy Technol 8(8):1900826
13. Arinaga AM, Ziegelski MC, Marks TJ (2021) Alternative oxidants for the catalytic oxidative coupling of methane. Angew Chem Int Ed 60(19):10502–10514
14. Keller GE, Bhasin MM (1982) Synthesis of ethylene via oxidative coupling of methane I Determination of active catalysts. J Catal 73(1):9–19
15. Ren T, Patel M, Kornelis B (2006) Olefins from conventional and heavy feedstocks: energy use in steam cracking and alternative processes. Energy 31(4):425–451
16. Huang P, Zhao YH, Zhang J, Zhu Y, Sun YH (2013) Exploiting shape effects of La_2O_3 nanocatalysts for oxidative coupling of methane reaction. Nanoscale 5(22):10844–10848
17. Jiang T, Song JJ, Huo MF, Yang NT, Liu JW, Zhang J, Sun YH, Zhu Y (2016) La_2O_3 catalysts with diverse spatial dimensionality for oxidative coupling of methane to produce ethylene and ethane. RSC Adv 6(41):34872–34876
18. Fu B, Jiang T, Zhu Y (2018) Structural effect of one-dimensional samarium oxide catalysts on oxidative coupling of methane. J Nanosci Nanotechnol 18(5):3398–3404
19. Sun YN, Shen Y, Song JJ, Ba RB, Huang SS, Zhao YH, Zhang J, Sun YH, Zhu Y (2016) Facet-controlled CeO_2 nanocrystals for oxidative coupling of methane. J Nanosci Nanotechnol 16(5):4692–4700
20. Takenaka S, Kaburagi T, Yamanaka I, Otsuka K (2001) Oxidative coupling of methane over Li^+-added Y_2O_3 catalyst prepared from $Y(OH)_3$. Catal Today 71(1–2):31–36
21. Papa F, Luminita P, Osiceanu P, Birjega R, Akane M, Balint I (2011) Acid-base properties of the active sites responsible for C_2^+ and CO_2 formation over MO–Sm_2O_3 (M = Zn, Mg, Ca and Sr) mixed oxides in OCM reaction. J Mol Catal A 346(1–2):46–54
22. Song JJ, Sun YN, Ba RB, Huang SS, Zhao YH, Sun YH, Zhu Y (2015) Monodisperse Sr–La_2O_3 hybrid nanofibers for oxidative coupling of methane to synthesize C_2 hydrocarbons. Nanoscale 7(6):2260–2264
23. Ferreira VJ, Tavares P, Figueiredo JL, Faria JL (2012) Effect of Mg, Ca, and Sr on CeO_2 based catalysts for the oxidative coupling of methane: Investigation on the oxygen species responsible for catalytic performance. Ind Eng Chem Res 51(32):10535–10541
24. Fan YQ, Sun MX, Miao CX, Yue YH, Hua WM, Gao Z (2021) Morphology effects of nanoscale Er_2O_3 and Sr-Er_2O_3 catalysts for oxidative coupling of methane. Catal Lett 151(8):2197–2206

25. Fan YQ, Miao CX, Yue YH, Hua WM, Gao Z (2021) Nanosheet-like Ho_2O_3 and Sr-Ho_2O_3 catalysts for oxidative coupling of methane. Catalysts 11(3):388
26. Haneda M, Tanaka M, Doi Y, Bion N (2018) Oxidative coupling of methane over Ba-doped Y_2O_3 catalyst-Similarity with active site for direct decomposition of NO. Mol Catal 457:74−81
27. Long RQ, Wan HL (1997) Oxidative coupling of methane over SrF_2/Y_2O_3 catalyst. Appl Catal A 159(1–2):45–58
28. Heneda M, Katsuragawa Y, Nakamura Y, Towata A (2018) Promoting effect of cerium oxide on the catalytic performance of yttrium oxide for oxidative coupling of methane. Front Chem 6:581
29. Zhao MQ, Ke SC, Wu HQ, Xia WS, Wan HL (2019) Flower-like Sr-La_2O_3 microspheres with hierarchically porous structures for oxidative coupling of methane. Ind Eng Chem Res 58(51):22847–22856
30. Kharas KCC, Lunsford JH (1989) Catalytic partial oxidation of methane over barium metaplumbate $BaPbO_3$: possible involvement of peroxide ion. J Am Chem Soc 111(6):2336–2337
31. Peng XD, Richards DA, Stair PC (1990) Surface composition and reactivity of lithium-doped magnesium oxide catalysts for oxidative coupling of methane. J Catal 121(1):99–109
32. Ding WP, Chen Y, Fu XC (1994) Oxidative coupling of methane over Ce^{4+}-doped Ba_3WO_6 catalysts: investigation on oxygen species responsible for catalytic performance. Catal Lett 23(1–2):69–78
33. Hou YH, Han WC, Xia WS, Wan HL (2015) Structure sensitivity of $La_2O_2CO_3$ catalysts in the oxidative coupling of methane. ACS Catal 5(3):1663–1674
34. Bai Y, Xia WS, Weng WZ, Lian MS, Zhao MQ, Wan HL (2018) Influence of phosphate on La-based catalysts for oxidative coupling of methane. Chem J Chin Univ Chin 39(2):247–254
35. Sayle TXT, Parker SC, Sayle DC (2005) Oxidising CO to CO_2 using ceria nanoparticles. Phys Chem Chem Phys 7(15):2936–2941
36. Spinicci R, Tofanari A (1990) Characterization of catalysts for methane-coupling by means of temperature programmed desorption. Catal Today 6(4):473–479
37. Xu J, Zhang Y, Xu X, Fang X, Xi R, Liu Y, Zheng R, Wang X (2019) Constructing $La_2B_2O_7$ (B = Ti, Zr, Ce) compounds with three typical crystalline phases for the oxidative coupling of methane: The effect of phase structures, superoxide anions, and alkalinity on the reactivity. ACS Catal 9(5):4030–4045
38. McFarland EW, Metiu H (2013) Catalysis by doped oxides. Chem Rev 113(6):4391–4427
39. Liang Q, Wu X, Weng D, Xu H (2008) Oxygen activation on Cu/Mn−Ce mixed oxides and the role in diesel soot oxidation. Catal Today 139(1–2):113–118
40. Elkins TW, Roberts SJ, Hagelin-Weaver HE (2016) Effects of alkali and alkaline-earth metal dopants on magnesium oxide supported rare-earth oxide catalysts in the oxidative coupling methane. Appl Catal A 528:175–190
41. Driscoll DJ, Martir W, Wang JX, Lunsford JH (1985) Formation of gas-phase methyl radicals over MgO. J Am Chem Soc 107(1):58–63
42. Bernal S, Blanco G, El Amarti A, Cifredo G, Fitian L, Galtayries A, Martín J, Pintado JM (2006) Surface basicity of ceria-supported lanthana. Influence of the calcination temperature. Surf Interface Anal 38(4):229–233
43. Peng L, Xu J, Fang X, Liu W, Xu X, Liu L, Li Z, Peng H, Zheng R, Wang X (2018) SnO_2 based catalysts with low-temperature performance for oxidative coupling of methane: Insight into the promotional effects of alkali-metal oxides. Eur J Inorg Chem 17:1787–1799
44. Xu J, Peng L, Fang X, Fu Z, Liu W, Xu X, Peng H, Zheng R, Wang X (2018) Developing reactive catalysts for low temperature oxidative coupling of methane: on the factors deciding the reaction performance of $Ln_2Ce_2O_7$ with different rare earth A sites. Appl Catal A 552:117–128
45. Xu J, Zhang Y, Liu Y, Fang X, Xu X, Liu W, Zheng R, Wang X (2019) Optimizing the reaction performance of $La_2Ce_2O_7$-based catalysts for oxidative coupling of methane (OCM) at lower temperature by lattice doping with Ca cations. Eur J Inorg Chem 2:183–194
46. Wang Z, Zou G, Luo X, Liu H, Gao R, Chou L, Wang X (2012) Oxidative coupling of methane over $BaCl_2$-TiO_2-SnO_2 catalyst. J Nat Gas Chem 21(1):49–55
47. Cheng F, Yang J, Yan L, Zhao J, Zhao HH, Song HL, Chou LJ (2018) Impact of chloride ions on the oxidative coupling of methane over Li/SnO_2 catalyst. React Kinet Mech Catal 125(2):675–688
48. Bernal S, Botana FJ, Garcia R, Rodiguez-Izquierdo JM (1987) Behaviour of rare earth sesquioxides exposed to atmospheric carbon dioxide and water. React Soliak 4(1–2):23–40
49. Djerdj I, Garnweitner G, Su DS, Niederberger M (2007) Morphology-controlled nonaqueous synthesis of anisotropic lanthanum hydroxide nanoparticles. J Solid State Chem 180(7):2154–2165

50. Farrukh MA, Imran F, Ali S, Khaleeq-ur-Rahman M, Naqvi II (2015) Micelle assisted synthesis of La_2O_3 nanoparticles and their applications in photodegradation of bromophenol blue. Russ J Appl Chem 88(9):1523–1527
51. Ito T, Wang JX, Lin CH, Lunsford JH (1985) Oxidative dimerization of methane over a lithium-promoted magnesium oxide catalyst. J Am Chem Soc 107(18):5062–5068
52. Yamashita H, Machida Y, Tomita A (1991) Oxidative coupling of methane with peroxide ions over barium-lanthanum-oxygen mixed oxide. Appl Catal A 79(2):203–214
53. Sollier BM, Bonne M, Khenoussi N, Michelin L, Miró EE, Gómez LE, Boix AV, Lebeau B (2020) Synthesis and characterization of electrospun nanofibers of Sr-La-Ce oxides as catalysts for the oxidative coupling of methane. Ind Eng Chem Res 59(25):11419–11430